Dalton Transactions

ROYAL SOCIETY OF CHEMISTRY

PAPER

View Article Online
View Journal | View Issue

Cite this: *Dalton Trans.*, 2026, **55**, 4802

Structural transformation and redox chemistry of Pd/CeO_2 during SO_2-induced sulfurization: an *in situ* XAFS study

Saki Shigenobu, [a] Takeharu Sugiyama, [b] Hajime Hojo [c] and Hisahiro Einaga *[c]

In situ X-ray absorption fine structure (XAFS) spectroscopy was employed to elucidate the structural evolution of Pd/CeO_2 catalysts during SO_2-induced sulfurization. Linear combination fitting of Ce L_3-edge XANES spectra quantified the $Ce^{4+} \rightarrow Ce^{3+}$ transformation, revealing fundamentally different sulfurization mechanisms for bare *versus* Pd-promoted CeO_2. At 500 °C, bare CeO_2 exhibited surface-limited sulfurization with $Ce^{3+}/(Ce^{3+} + Ce^{4+})$ reaching 0.18, while Pd/CeO_2 achieved 0.68, demonstrating bulk oxygen participation. Temperature-dependent measurements (200–500 °C) confirmed thermal activation of the sulfurization process, with higher temperatures enabling deeper lattice penetration. Complementary Pd L_3-edge XANES revealed that Pd maintained its oxidized state throughout SO_2 exposure, excluding PdS formation. S K-edge analysis confirmed exclusive SO_4^{2-} formation *via* direct oxidation without intermediate species. These findings establish that Pd catalyzes oxygen mobility within the CeO_2 lattice, transforming sulfurization from a surface-confined to a bulk-accessible process while preserving the fluorite structure. The resulting cerium sulfate oxide ($Ce_2O_2SO_4$) exhibits enhanced stability against re-oxidation in Pd/CeO_2, contrasting with the partial reversibility observed for bare CeO_2.

Received 11th January 2026,
Accepted 27th February 2026

DOI: 10.1039/d6dt00070c

rsc.li/dalton

1. Introduction

Pd catalysts are key materials for purifying exhaust gases from factories and vehicles.[1–4] These gases contain air pollutants and harmful compounds, such as NOx, CO, and hydrocarbons. Regulations on these compounds are becoming increasingly stringent worldwide to achieve a sustainable society. Generally, platinum-group metal (PGM) catalysts are used to oxidize or reduce harmful compounds to non-toxic substances. There is a strong need to reduce the amount of PGM used because they are scarce and expensive. Therefore, the activity of PGM catalysts must be improved. It has been reported that Pd has better thermal durability than Pt.[1,5–7] Various oxides, such as Al_2O_3, SiO_2, and TiO_2, have been used as supports for Pd catalysts. CeO_2 has excellent redox properties and improves CO oxidation activity at low temperatures when used as a supporting material for Pd catalysts. Therefore, CeO_2-supported Pd catalysts (Pd/CeO_2) are frequently used for oxidation reactions.

Catalyst poisoning by sulfur-containing substances (*e.g.*, SO_2 and H_2S) poses a critical challenge in exhaust gas purification. SO_2, ubiquitously emitted from both stationary and mobile sources, can be converted to H_2S under reducing conditions, creating multiple pathways for sulfur poisoning. This sulfur exposure severely deteriorates the performance of Pd catalysts.[8–12] Therefore, developing Pd catalysts with both high activity and enhanced sulfur tolerance is imperative. A thorough understanding of the sulfur poisoning mechanism is essential for the rational design of such S-tolerant catalysts.

It has been reported that treatment of supported Pd catalysts with SO_2 generally leads to a significant decrease in catalytic activity, primarily due to palladium sulfidation and a reduction in catalyst surface area.[11,13–16] The effects of SO_2 treatment on the properties of CeO_2 have also been investigated.[17–19] When CeO_2 undergoes sulfurization, oxygen vacancies are introduced, resulting in the reduction of Ce^{4+} to Ce^{3+}. Sulfurized CeO_2 formed by SO_2 treatment exhibits enhanced oxygen storage capacity and high activity for the reduction of nitrogen oxides by ammonia.[20]

Although Pd/CeO_2 catalysts suffer from activity deterioration in the presence of SO_2, Hilaire *et al.* reported that SO_2 poisoning, under alternating CO and O_2 pulse conditions, unexpectedly increased the amount of oxygen that could be transferred to and from the catalyst across the entire temperature range examined.[21] These findings highlight the complex-

[a]*Department of Molecular and Material Sciences, Graduate School of Engineering Sciences, Kyushu University, 6-1, Kasugakoen, Kasuga, Fukuoka 816-8580, Japan*
[b]*Research Center for Synchrotron Light Application, Kyushu University, 6-1, Kasugakoen, Kasuga, Fukuoka 816-8580, Japan*
[c]*Department of Advanced Materials Science and Engineering, Faculty of Engineering Sciences, Kyushu University, 6-1, Kasugakoen, Kasuga, Fukuoka 816-8580, Japan. E-mail: einaga.hisahiro.399@m.kyushu-u.ac.jp*

ity of sulfur poisoning behavior in CeO_2-supported Pd catalysts. Despite these insights, most previous investigations have been conducted under *ex situ* conditions or have focused solely on catalytic performance evaluation. Consequently, the real-time structural evolution of Pd/CeO_2 during SO_2 exposure and the specific role of Pd in promoting CeO_2 sulfurization remain insufficiently understood. Addressing these knowledge gaps is essential for developing sulfur-tolerant Pd-based catalysts.

In this study, we employed *in situ* XAFS measurements under controlled SO_2 gas flow to capture the dynamic structural changes of both Pd and CeO_2 components in real time. This approach enables us to directly observe the sequential transformation of Ce oxidation states (Ce^{4+} to Ce^{3+}) during SO_2 exposure, simultaneously monitor the chemical state of Pd species to clarify whether $PdSO_4$ or PdS formation occurs under our reaction conditions, quantitatively determine the Ce^{3+}/Ce^{4+} ratio evolution as a function of time and temperature, and elucidate the promotional effect of Pd on CeO_2 sulfurization through comparative studies of Pd/CeO_2 *versus* bare CeO_2. Our *in situ* approach, combined with complementary *ex situ* characterization (XRD, STEM-EDS, XPS), provides unprecedented insights into the sulfurization mechanism and helps explain the paradoxical enhancement of oxygen storage capacity reported by Hilaire *et al.* This mechanistic understanding is crucial for designing next-generation sulfur-tolerant catalysts.

Unlike previous studies that primarily relied on *ex situ* characterization or focused on catalytic performance under SO_2 exposure, our work provides the first comprehensive *in situ* XAFS investigation of Pd/CeO_2 sulfurization under controlled reaction conditions. This real-time approach enables direct observation of Ce oxidation state evolution and Pd speciation during SO_2 treatment, revealing the mechanistic role of Pd in promoting bulk oxygen mobility and irreversible sulfate formation. By combining Ce L_3-, Pd L_3-, and S K-edge analyses with complementary structural characterization, we uncover a fundamental shift in sulfurization behavior—from surface-limited in bare CeO_2 to bulk-accessible in Pd/CeO_2—thus offering unprecedented insights into the design of sulfur-tolerant Pd-based catalysts.

2. Experimental

2.1 Catalyst preparation

Pd/CeO_2 catalysts were prepared by the impregnation method. CeO_2 (JRC-CEO-5, Catalysis Society of Japan, 99.98% purity) was used as the support. The pore volume of JRC-CEO-5 CeO_2 determined by N_2 adsorption was 0.24 mL cm^{-3} g^{-1}. An aqueous solution of tetraamminepalladium(II) nitrate, $[Pd(NH_3)_4](NO_3)_2$ (10 wt% in H_2O, Sigma-Aldrich Japan, purity: 99.99%) was added dropwise to CeO_2 powder. The amount of $[Pd(NH_3)_4](NO_3)_2$ solution was adjusted to achieve a Pd loading of 1 wt%. The impregnation was carried out in a water bath at 60 °C, followed by thorough mixing and drying. The precursor was dried at 100 °C overnight, calcined in air at 400 °C for 2 h, and subsequently reduced under a 5% H_2–N_2 flow at 200 °C for 1 h. The final Pd loading was 1 wt%.

2.2 Catalyst characterization

X-ray diffraction (XRD) patterns were recorded using a RINT 2200 diffractometer (Rigaku, Japan) with Cu Kα radiation (λ = 1.54 Å) at 40 kV and 20 mA, with a step rate of 2° min^{-1}. Temperature-programmed reduction with H_2 (H_2-TPR) was performed using a BEL-CAT instrument (Microtrac BEL). Samples (0.10 g) were pretreated in air at 350 °C for 1 h, then heated from 50 to 950 °C at 5 °C min^{-1}. X-ray photoelectron spectroscopy (XPS) was carried out using a Kratos ESCA-3400 spectrometer (AXIS-165, KRATOS, Japan) with an Al Kα source. X-ray fluorescence (XRF) spectra were obtained using a ZSX Primus IV/RX9 instrument (Rigaku).

2.3 *In situ* XAFS measurements

XAFS measurements were conducted at the Kyushu Synchrotron Light Research Center (SAGA-LS), beamline BL06 (Saga, Japan). The storage ring energy was 1.4 GeV, and a Si (111) double-crystal monochromator was employed. Ce L_3-edge spectra were collected in transmission mode, while S K-edge and Pd L_3-edge spectra were recorded in fluorescence mode. For *in situ* measurements, catalysts were mixed with boron nitride, pressed into 10 mm diameter disks, and placed in a glass cell (Fig. S1). The samples were heated to the reaction temperature under a 500 ppm SO_2–N_2 flow (100 mL min^{-1}), then measured at room temperature. Subsequently, the catalysts were reoxidized in O_2 at 500 °C and re-measured. Additional measurements were performed at 200 °C and 400 °C under the same conditions. XAFS data analysis was carried out using the Athena software package.[22] CeO_2 (JRC-CEO-5, Catalysis Society of Japan, 99.98% purity) and $Ce(NO_3)_3$ (Kojundo Chemical Lab. Co., Ltd, 99.9% purity) were used as reference samples.

3. Results and discussion

3.1 Structural changes in CeO_2 support induced by SO_2 treatment

Fig. 1 presents the *in situ* Ce L_3-edge XANES spectra of CeO_2 and Pd/CeO_2 during SO_2 treatment at 500 °C. In the fresh samples, characteristic peaks corresponding to quasi-atomic Ce $2p_{3/2} \rightarrow 5d_{5/2,3/2}$ electronic transitions[23–25] were observed at 5730 and 5737 eV, confirming the predominance of Ce^{4+} in both materials. The similarity between the spectra of Pd/CeO_2 and bare CeO_2 indicates that Pd loading did not alter the initial oxidation state of Ce. Upon exposure to SO_2, both samples exhibited a gradual decrease in peak intensities at 5730 and 5737 eV, accompanied by a shift of the absorption edge (Fig. 1(b)). Notably, Pd/CeO_2 displayed more pronounced spectral changes, including the emergence of a distinct peak at 5726 eV characteristic of Ce^{3+}, demonstrating that Pd significantly enhances CeO_2 reduction under SO_2. The presence of

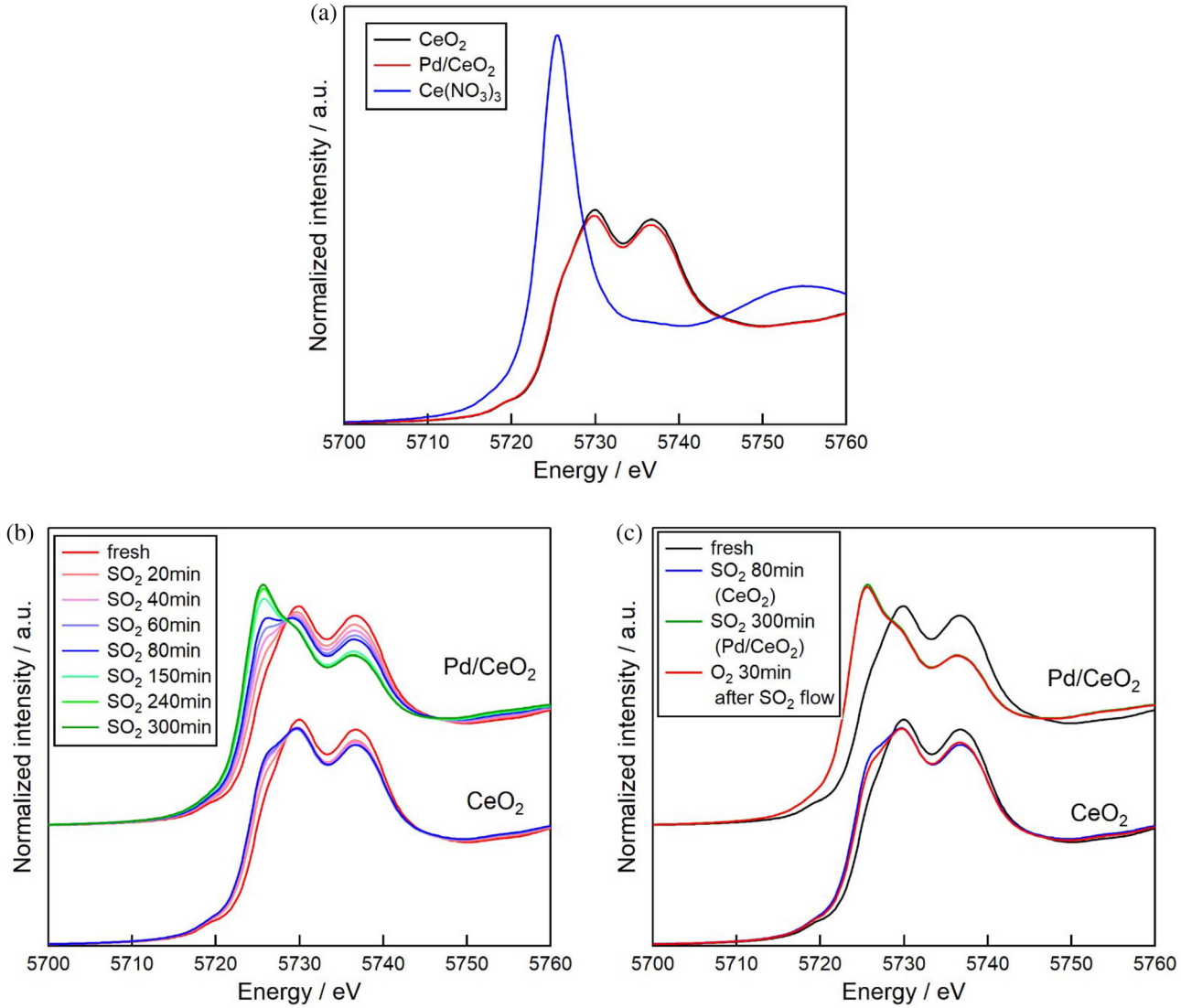

Fig. 1 *In situ* Ce L_3-edge XANES spectra of CeO_2 and Pd/CeO_2 at 500 °C. (a) Fresh samples before SO_2 exposure. (b) Under SO_2 flow (500 ppm, 100 mL min^{-1}) for up to 300 min. (c) After switching to O_2 flow at 500 °C following SO_2 treatment.

isosbestic points in both samples confirms direct conversion of Ce^{4+} to Ce^{3+} without detectable intermediates.

Quantitative analysis of the Ce oxidation states was performed using two complementary approaches. First, the XANES spectra were deconvoluted using arctangent and Gaussian functions (Fig. 2), yielding four components: peaks A, B, and D (Ce^{4+}) and peak C (Ce^{3+}). The $Ce^{3+}/(Ce^{3+}+Ce^{4+})$ ratio was calculated from the integrated peak areas. In pristine CeO_2, Ce^{3+} arises from intrinsic oxygen vacancies; however, its absolute concentration depends significantly on preparation conditions and fitting procedures.[26–28] To validate these results, linear combination fitting (LCF) analysis was conducted using CeO_2 and $Ce(NO_3)_3$ as Ce^{4+} and Ce^{3+} references, respectively (Fig. 3). While this method cannot quantify intrinsic Ce^{3+} in pure CeO_2, it provides reliable assessment of SO_2-induced changes. The temporal evolution of $Ce^{3+}/(Ce^{3+} + Ce^{4+})$ ratios (Fig. 4) was monitored throughout SO_2 exposure and subsequent O_2 reoxidation. For bare CeO_2, measurements were taken at 0, 20, 40, 60, and 80 min under SO_2 flow, followed by O_2 treatment at 500 °C. For Pd/CeO_2, data points were collected at 0, 20, 40, 60, 80, 150, 240, and 300 min during continuous SO_2 exposure, after which the gas was switched to O_2 for reoxidation. These time intervals correspond exactly to the horizontal axis in Fig. 4, ensuring direct comparison between the two catalysts. Bare CeO_2 reached a plateau at $Ce^{3+}/(Ce^{3+} + Ce^{4+}) = 0.18$ after 60 min, whereas Pd/CeO_2 continued reducing to $Ce^{3+}/(Ce^{3+} + Ce^{4+}) = 0.68$ after 300 min, highlighting the catalytic role of Pd in CeO_2 sulfurization.

Upon switching from SO_2 to O_2 flow at 500 °C, the XANES spectra revealed distinct re-oxidation behaviors (Fig. 1(c)). Bare CeO_2 exhibited partial recovery of the Ce^{4+} state, as evidenced by the diminished Ce^{3+} peak intensity, indicating reversible

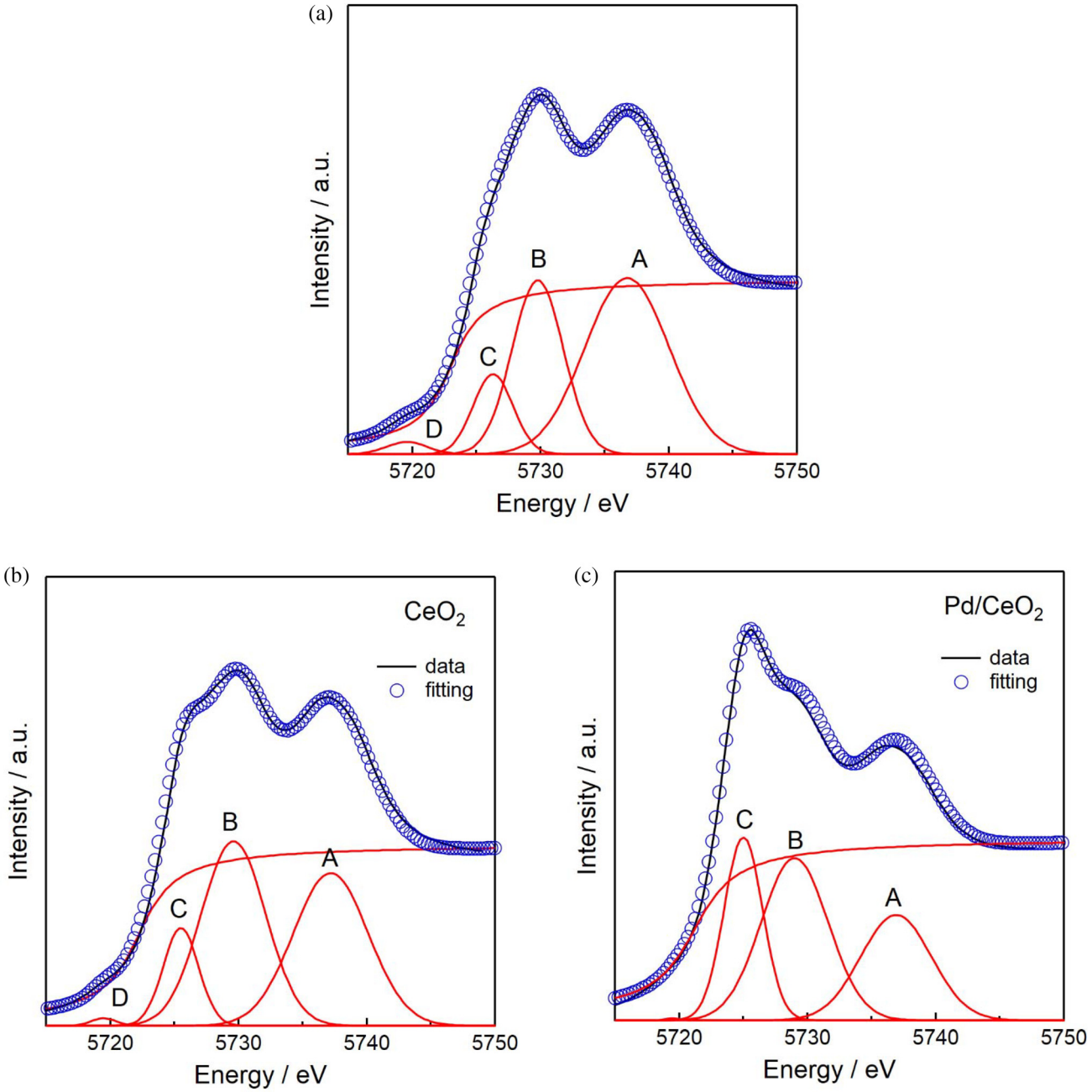

Fig. 2 Ce L_3-edge XANES spectra and peak fitting for Ce oxidation states. (a) Fresh CeO_2. (b) CeO_2 after 80 min under SO_2 flow at 500 °C. (c) Pd/CeO_2 after 300 min under SO_2 flow at 500 °C.

reduction of surface sites. In contrast, Pd/CeO_2 showed no spectral changes during O_2 treatment, demonstrating that Pd stabilizes the sulfurized state and prevents re-oxidation. The absence of re-oxidation also excludes the formation of bulk Ce_2O_3 during SO_2 treatment, as Ce_2O_3 would readily re-oxidize to CeO_2 under these oxidizing conditions.

Fig. 5 presents the *in situ* Ce L_3-edge EXAFS spectra of CeO_2 and Pd/CeO_2 collected at 500 °C under SO2 flow. Both samples initially displayed characteristic coordination shells: Ce–O at 2.0 Å and Ce–(O)–Ce at 3.5 Å (phase uncorrected). Progressive SO_2 exposure induced time-dependent attenuation of both peaks, reflecting the disruption of local structural order in the CeO_2 lattice. Notably, after 40 min of SO_2 treatment, Pd/CeO_2 exhibited significantly greater structural disorder than bare CeO_2, as evidenced by the more pronounced reduction in Ce–O and Ce–(O)–Ce peak intensities. Subsequent O_2 treatment revealed contrasting structural recovery behaviors. While bare CeO_2 showed partial restoration of the Ce–O coordination shell, consistent with the $Ce^{3+} \rightarrow Ce^{4+}$ re-oxidation observed in XANES (Fig. 1), Pd/CeO_2 remained structurally unchanged.

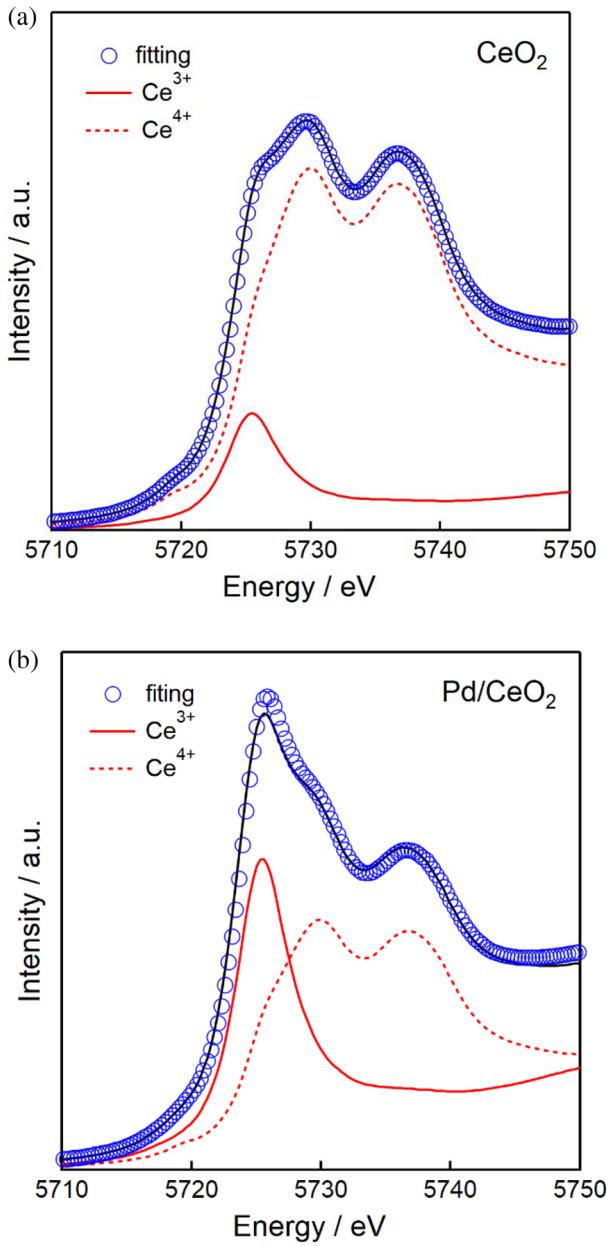

Fig. 3 Linear combination fitting (LCF) of Ce L_3-edge XANES spectra using CeO_2 and $Ce(NO_3)_3$ references. (a) CeO_2 after 80 min SO_2 exposure at 500 °C. (b) Pd/CeO_2 after 300 min SO_2 exposure at 500 °C.

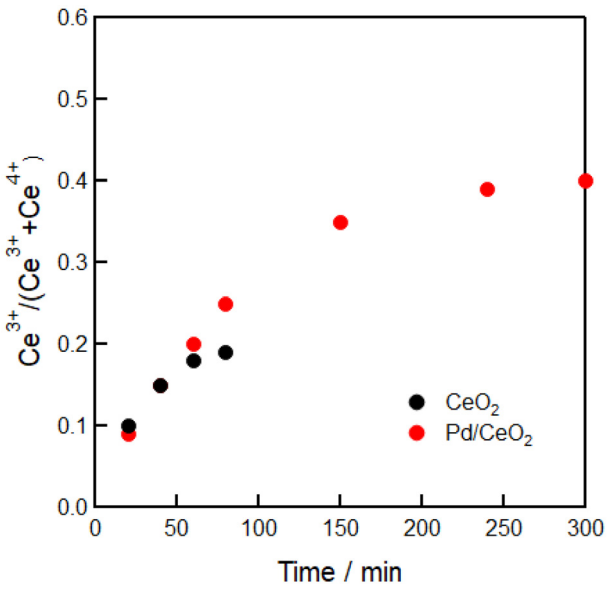

Fig. 4 Time-dependent evolution of $Ce^{3+}/(Ce^{3+} + Ce^{4+})$ ratio for bare CeO_2 and Pd/CeO_2 during SO_2 exposure at 500 °C, followed by O_2 re-oxidation. CeO_2 was measured at 0, 20, 40, 60, and 80 min under SO_2 flow, then switched to O_2 at 500 °C. Pd/CeO_2 was measured at 0, 20, 40, 60, 80, 150, 240, and 300 min under SO_2 flow, followed by O_2 treatment at 500 °C.

This irreversibility demonstrates that Pd not only accelerates CeO_2 sulfurization but also stabilizes the resulting disordered structure against re-oxidation, likely through the formation of stable sulfate species at the Pd–CeO_2 interface.

The temperature dependence of SO_2-induced CeO_2 reduction was investigated systematically (Fig. 6). At 400 °C, the Ce L_3-edge XANES spectra exhibited a characteristic red-shift of the absorption edge accompanied by diminished Ce^{4+} peak intensity, confirming partial reduction to Ce^{3+}. The presence of clear isosbestic points demonstrated that direct $Ce^{4+} \rightarrow Ce^{3+}$ conversion occurred without intermediates, similar to the 500 °C treatment. However, quantitative analysis revealed a lower $Ce^{3+}/(Ce^{3+}+Ce^{4+})$ ratio compared to 500 °C, establishing a positive correlation between reaction temperature and reduction extent. At 200 °C, minimal spectral changes were observed even after prolonged SO_2 exposure, suggesting that sulfurization was confined to the outermost surface layer under these mild conditions. These results demonstrate that CeO_2 sulfurization exhibits strong thermal activation, with higher temperatures required to enable SO_2 penetration beyond the surface region into the bulk lattice.

To elucidate the role of Pd in CeO_2 reduction, comparative H_2-reduction experiments were conducted at 600 °C (Fig. 7(a)). This temperature was selected based on established H_2-TPR profiles showing distinct reduction regimes: surface oxygen removal (50–600 °C) and bulk oxygen extraction (600–950 °C).[29,30] Therefore, treatment at 600 °C enables selective monitoring of surface reduction processes. Both CeO_2 and Pd/CeO_2 exhibited comparable shifts in their absorption edges during H_2 treatment, with linear combination fitting revealing identical Ce^{3+} formation (15% conversion from Ce^{4+}) in both samples. This equivalence contrasts sharply with the SO_2-treatment results, where Pd dramatically enhanced CeO_2 reduction. The absence of Pd promotion under H_2 indicates that the catalytic effect is specific to SO_2-mediated reduction pathways, suggesting fundamentally different mechanistic routes for H_2 *versus* SO_2 reduction of CeO_2.

The structural consequences of H_2 reduction were examined *via in situ* Ce L_3-edge EXAFS (Fig. 7(b)). Both CeO_2 and Pd/CeO_2 displayed comparable attenuation of Ce–O and Ce–

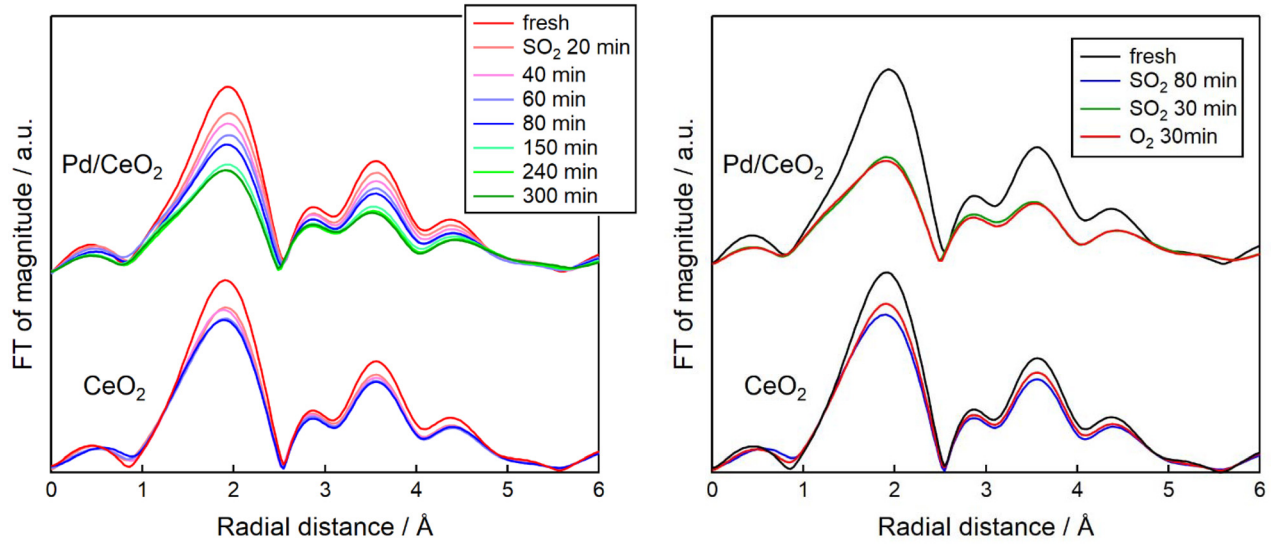

Fig. 5 *In situ* Ce L_3-edge EXAFS spectra of CeO_2 and Pd/CeO_2 during SO_2 exposure at 500 °C. CeO_2 measured at 0, 20, 40, 60, and 80 min; Pd/CeO_2 measured at 0, 20, 40, 60, 80, 150, 240, and 300 min under SO_2 flow (500 ppm, 100 mL min^{-1}).

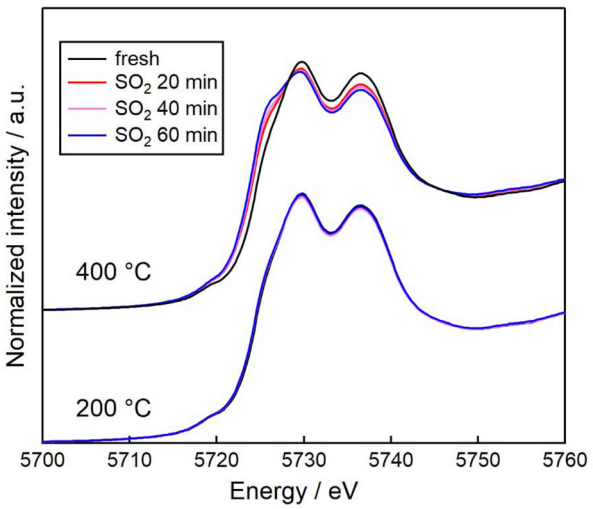

Fig. 6 Ce L_3-edge XANES spectra of CeO_2 and Pd/CeO_2 under SO_2 flow (500 ppm, 100 mL·min^{-1}) at 200 °C and 400 °C. Measurements taken at 0, 20, 40, and 60 min.

(O)–Ce coordination peaks at 600 °C, indicating similar degrees of local structural disorder upon surface oxygen removal. The equivalent post-reduction peak intensities confirm that while Pd accelerates the kinetics of CeO_2 reduction under certain conditions, it does not alter the final structural state of H_2-reduced CeO_2. This observation further supports that the promotional effect of Pd is reaction-specific rather than a general enhancement of CeO_2 reducibility.

The comparative analysis of H_2 and SO_2 reduction provides critical mechanistic insights into Pd's catalytic role. For bare CeO_2, SO_2 treatment at 500 °C yielded $Ce^{3+}/(Ce^{3+}+Ce^{4+})$ ratios identical to those achieved by H_2 reduction at 600 °C, demonstrating that SO_2-induced sulfate formation is confined to surface oxygen sites. This surface-limited reaction persisted even under prolonged SO_2 exposure, indicating an intrinsic barrier to bulk sulfurization in unpromoted CeO_2. In stark contrast, Pd/CeO_2 under SO_2 treatment surpassed the H_2-induced reduction threshold, unequivocally demonstrating SO_2 access to bulk oxygen sites. This fundamental difference reveals that Pd not only accelerates surface sulfurization kinetics but, more importantly, enables SO_2 penetration into the CeO_2 bulk lattice. The mechanism likely involves Pd-mediated oxygen mobility enhancement or the creation of preferential SO_2 diffusion pathways at the Pd–CeO_2 interface, fundamentally altering the sulfurization process from a surface-limited to a bulk-accessible reaction.

Surface chemical states were characterized by XPS to complement the bulk-sensitive XAFS measurements (Fig. 8). The Ce 3d spectra exhibited the characteristic multiplet structure with V ($3d_{5/2}$) and U ($3d_{3/2}$) components and their satellites (V′, V″, V‴, U′, U″, U‴).[31–34] Fresh samples displayed predominantly Ce^{4+}-associated features, while SO_2-treated Pd/CeO_2 showed pronounced enhancement of the Ce^{3+} markers (U′ and V′ peaks).[31,34] Quantitative deconvolution yielded Ce^{3+}/Ce^{4+} = 0.31/0.69, in reasonable agreement with the XANES-derived values. Given the XPS probing depth of approximately 2 nm in CeO_2,[38,39] these results confirm substantial Ce^{3+} enrichment within the near-surface region. The coexistence of Ce^{4+} and Ce^{3+} in this shallow sampling volume indicates incomplete surface sulfurization, suggesting either heterogeneous reaction sites or equilibrium between sulfurized and pristine surface domains.

XRD analysis was employed to assess crystallographic changes induced by SO_2 treatment (Fig. 9). Fresh Pd/CeO_2 exhibited characteristic reflections of the fluorite structure at 2θ = 28, 33, 47, 56, 59, 69, 76, 79, 88, and 95°, consistent with

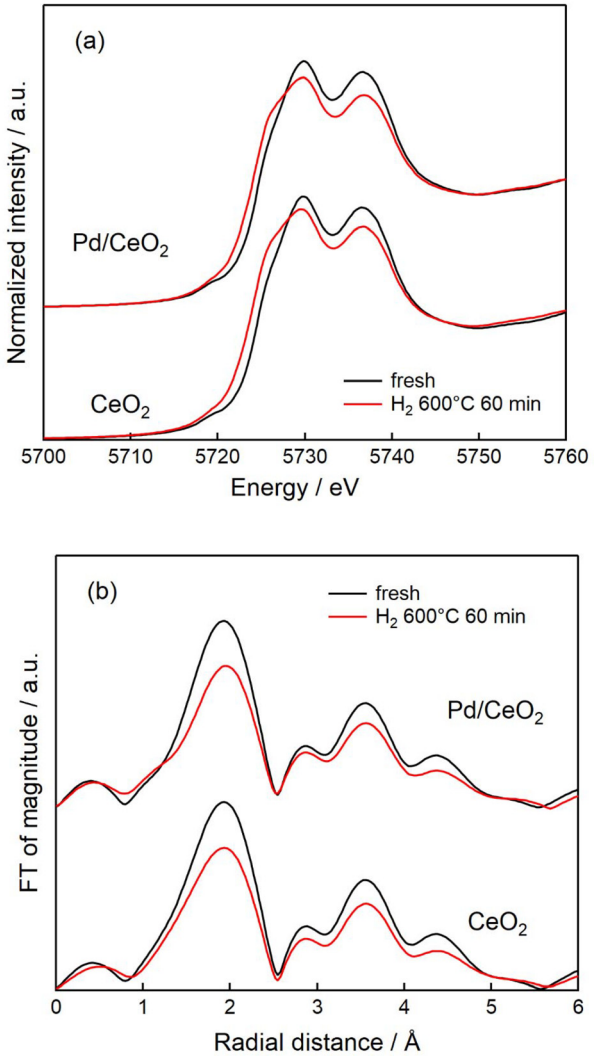

Fig. 7 (a) Ce L_3-edge XANES and (b) EXAFS spectra of CeO_2 and Pd/CeO_2 during H_2 reduction at 600 °C (5% H_2–N_2 flow, 100 mL min^{-1}). Measurements taken after 60 min of H_2 exposure.

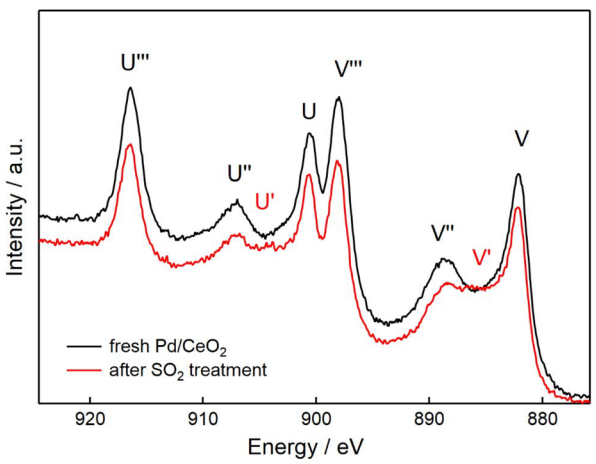

Fig. 8 XPS spectra of Pd/CeO_2 before and after SO_2 treatment at 500 °C (500 ppm SO_2, 100 mL min^{-1}, 300 min). Spectra show Ce 3d multiplet structure and changes in Ce^{3+}/Ce^{4+} ratio upon sulfurization.

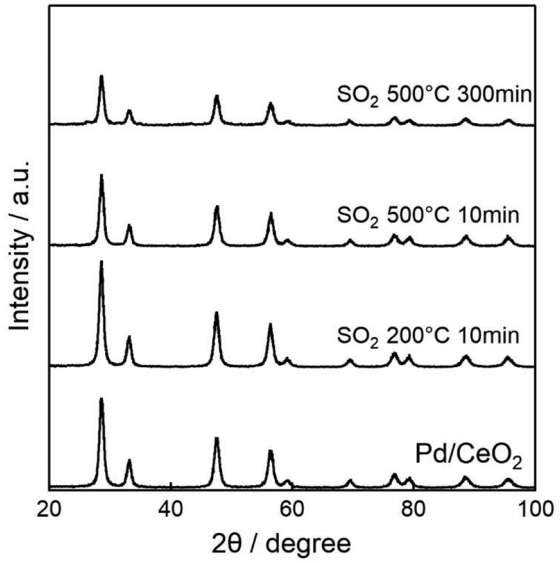

Fig. 9 XRD patterns of Pd/CeO_2 before and after SO_2 exposure at 500 °C (500 ppm SO_2, 100 mL min^{-1}, 300 min). Fluorite structure reflections are retained with intensity attenuation, indicating increased disorder without phase transformation.

cubic CeO_2 ($Fm\bar{3}m$).[35] The absence of Pd or PdO reflections confirms high metal dispersion on the CeO_2 support. Following SO_2 treatment, the fluorite reflections showed reduced intensities while maintaining their positions, with no emergence of new phases. This intensity attenuation without peak shifting or phase transformation indicates partial amorphization or increased structural disorder rather than formation of crystalline sulfate phases. The preservation of the fluorite framework despite SO_2-induced reduction aligns with the EXAFS observations of decreased local ordering while maintaining the basic CeO_2 structure.

In this study, the Pd/CeO_2 catalyst was subjected to calcination in air at 400 °C, followed by reductive activation under 5% H_2/N_2 at 200 °C. To properly interpret the sulfurization behavior of Pd/CeO_2, it is important to consider the extent to which these thermal and reductive treatments may influence the CeO_2 support itself. Because the CeO_2 used in this work had already undergone high-temperature calcination at 600 °C prior to catalyst preparation, an additional calcination at 400 °C is unlikely to induce further structural modifications. Thus, the only treatment step that may affect the bare support is the mild reduction at 200 °C. According to previous H_2-TPR studies, CeO_2 exhibits negligible reduction at 200 °C, with only minimal $Ce^{4+} \rightarrow Ce^{3+}$ conversion and insignificant oxygen-vacancy formation.[29] These findings indicate that such mild reductive pre-treatment does not meaningfully alter the intrinsic redox properties of CeO_2. In contrast, H_2-TPR measurements demonstrate that the incorporation of Pd markedly enhances the reducibility of surface lattice oxygen in CeO_2. Therefore, the possibility that this Pd-induced increase in oxygen mobility facilitates the reaction with SO_2 cannot be excluded.

3.2 Changes in Pd on catalysts and the structure of sulfur species formed by SO_2

The Pd-CeO_2 interface plays a crucial role in catalytic performance, particularly for CO oxidation, where Pd deposition on CeO_2 dramatically enhances activity.[29,36,37] Since the Pd oxidation state directly governs interfacial reactivity, we monitored Pd speciation during SO_2 exposure using *in situ* Pd L_3-edge XANES (Fig. 10). The Pd L_3-edge spectra, originating from $2p_{3/2} \rightarrow 4d$ electronic transitions and thus sensitive to d-electron occupancy, remained invariant throughout SO_2 treatment at 500 °C. This spectral stability definitively excludes Pd reduction to metallic Pd^0 or conversion to PdS, indicating that Pd maintains its oxidized state despite the strongly reducing SO_2 atmosphere. This resistance to reduction contrasts markedly with the facile CeO_2 reduction observed under identical conditions, suggesting that SO_2 preferentially interacts with the CeO_2 support rather than the supported Pd species.

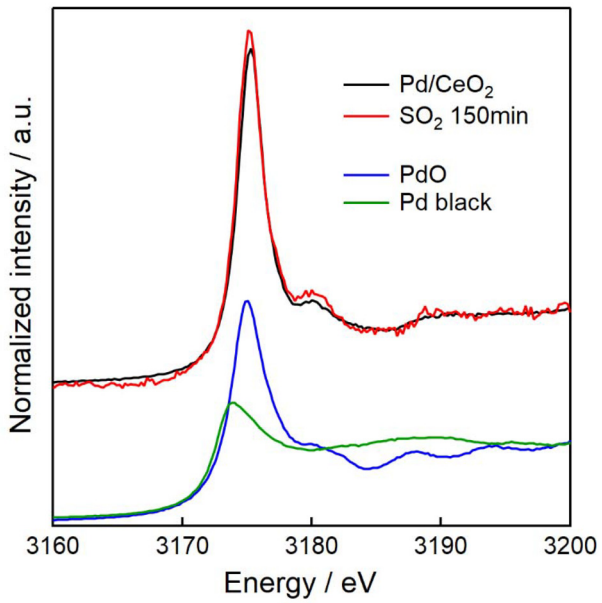

Fig. 10 *In situ* Pd L_3-edge XANES spectra of Pd/CeO_2 during SO_2 exposure at 500 °C (500 ppm SO_2, 100 mL min^{-1}) for up to 300 min. Spectra confirm Pd remains in oxidized state throughout sulfurization.

STEM-EDS mapping provided direct visualization of Pd dispersion and sulfur distribution before and after SO_2 treatment at 500 °C (Fig. 11). Fresh Pd/CeO_2 exhibited uniformly dispersed Pd nanoparticles with a mean diameter of ~3 nm and absence of large aggregates (>30 nm), consistent with the XRD results showing no detectable Pd or PdO reflections. Following SO_2 treatment, Pd maintained its original particle size distribution, demonstrating remarkable resistance to sintering under sulfurizing conditions. Critically, EDS mapping revealed homogeneous sulfur distribution across the entire catalyst surface, confirming uniform CeO_2 sulfurization rather than localized sulfate formation. This comprehensive surface sulfurization, combined with stable Pd dispersion, indicates that SO_2 interacts primarily with the CeO_2 support while leaving the metal nanoparticles structurally intact.

Sulfur speciation during SO_2 treatment was monitored *via in situ* S K-edge XANES spectroscopy (Fig. 12). Both CeO_2 and Pd/CeO_2 developed a dominant peak at 2.482 keV, characteristic of SO_4^{2-} species, which intensified over 60 min before reaching steady state. For bare CeO_2, a transient feature at 2.479 keV indicated initial SO_2 adsorption, which subsequently oxidized to S^{6+} within 60 min. In contrast, Pd/CeO_2 exclusively

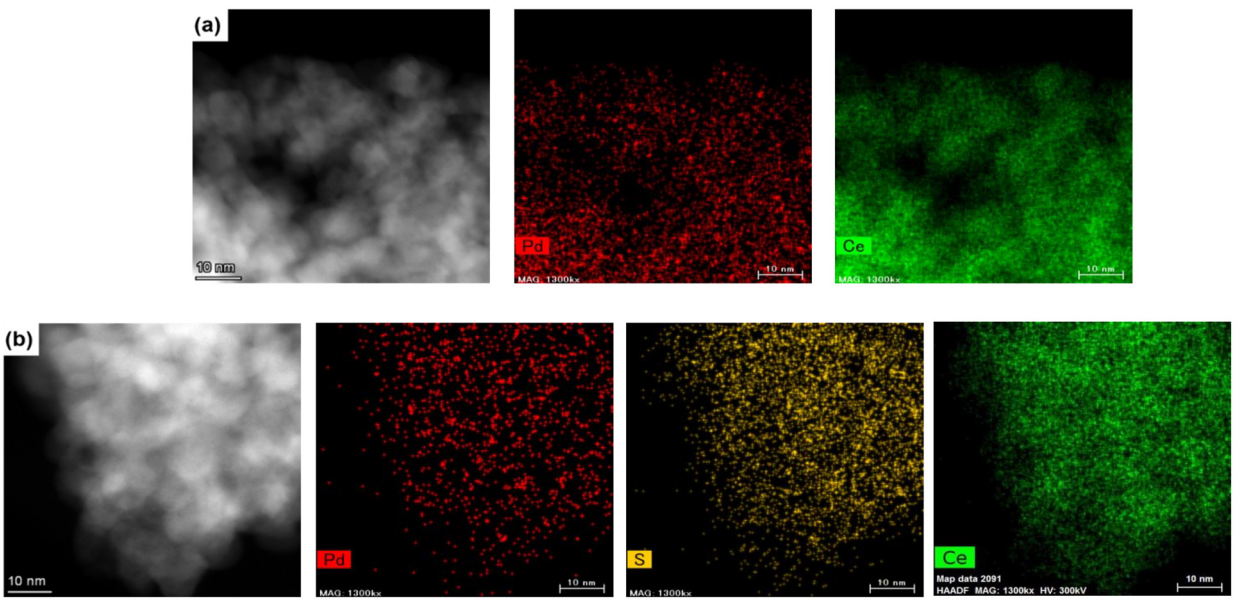

Fig. 11 STEM-EDS mapping of Pd/CeO_2 before and after SO_2 exposure at 500 °C (500 ppm SO_2, 100 mL min^{-1}, 300 min). (a) Fresh sample showing uniform Pd dispersion (~3 nm). (b) After SO_2 treatment, Pd particle size remains unchanged; sulfur is homogeneously distributed across the surface.

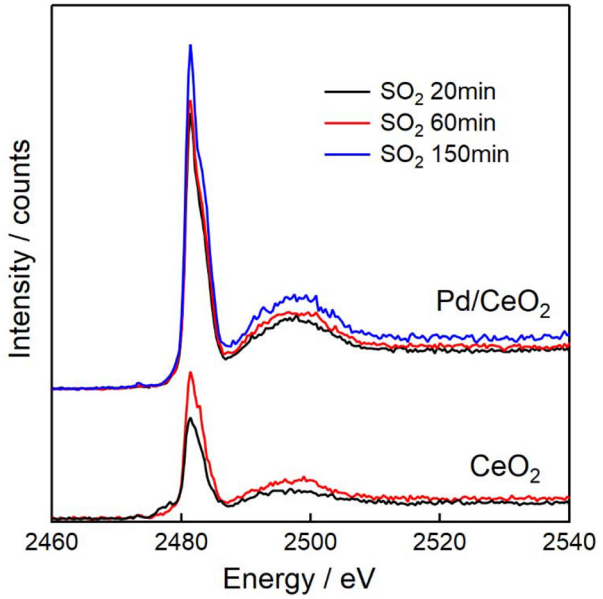

Fig. 12 *In situ* S K-edge XANES spectra of CeO_2 and Pd/CeO_2 during SO_2 exposure at 500 °C (500 ppm SO_2, 100 mL min^{-1}) for up to 60 min. Spectra show formation of SO_4^{2-} species; Pd/CeO_2 exhibits direct conversion without intermediate oxidation states.

formed SO_4^{2-} without detectable intermediate oxidation states, suggesting that Pd facilitates direct $SO_2 \rightarrow SO_4^{2-}$ conversion. These observations confirm that surface sulfate formation is the primary sulfurization pathway for both catalysts, with the key distinction being the reaction kinetics: Pd accelerates complete oxidation to sulfate while suppressing intermediate species formation. This direct sulfate formation mechanism explains the irreversible nature of Pd/CeO_2 sulfurization observed in the Ce L_3-edge XANES studies.

Diffuse-reflectance FTIR spectra collected for CeO_2 and Pd/CeO_2 before and after sulfation exhibit a broad absorption band near 1200 cm^{-1}, which is indicative of bulk-like sulfate species incorporated beneath the ceria surface (Fig. S2). This interpretation is consistent with previous findings showing that subsurface sulfate formation on ceria produces a broad feature around 1200 cm^{-1}, whereas surface sulfate species generate sharper bands in the 1340–1400 cm^{-1} region.[38] The predominance of the 1200 cm^{-1} band under the present conditions suggests that sulfation proceeds through partial reduction of Ce^{4+} to Ce^{3+} and subsequent migration of sulfate into near-surface layers. The comparatively stronger intensity of this band on Pd/CeO_2 implies that palladium enhances the redox activity and oxygen mobility of the ceria support, thereby promoting the incorporation of sulfate species into subsurface sites.

Quantitative sulfur analysis by XRF provided further insights into the extent of sulfurization (Table 1). The $Ce^{3+}/(Ce^{3+} + Ce^{4+})$ ratios were evaluated from these peak areas according to the reported literature. The $Ce^{3+}/(Ce^{3+} + Ce^{4+})$ ratios were calculated from the integrated peak areas based on

Table 1 Ce ion ratios calculated by linear combination fitting with standards and mol ratio of SO_3/CeO_2 calculated by XRF

	LCF fitting		Curve fitting		
	Ce^{3+}	Ce^{4+}	Ce^{3+}	Ce^{4+}	SO_3/CeO_2
Fresh CeO_2	0.00	1.00	0.11	0.89	—
CeO_2 after SO_2	0.15	0.85	0.14	0.86	0.09
CeO_2 after H_2	0.15	0.85	0.13	0.87	—
Fresh Pd/CeO_2	0.02	0.98	0.12	0.88	—
Pd/CeO_2 after SO_2	0.40	0.60	0.28	0.72	0.24
Pd/CeO_2 after H_2	0.15	0.85	0.13	0.87	—

established methods reported in the literature.[39] The S/CeO_2 molar ratios were 0.24 for Pd/CeO_2 *versus* 0.09 for bare CeO_2, demonstrating a 2.7-fold enhancement in sulfate formation with Pd promotion. This substantial difference correlates directly with the enhanced $Ce^{4+} \rightarrow Ce^{3+}$ reduction observed in XANES, confirming that Pd catalyzes both lattice oxygen extraction and subsequent sulfate formation. Notably, the Ce^{3+}/S molar ratio was approximately 1.7 for both catalysts, suggesting a stoichiometric relationship independent of Pd presence. This invariant ratio indicates that each sulfate formation event consumes a consistent number of lattice oxygen atoms, likely following the reaction: $2CeO_2 + SO_2 \rightarrow Ce_2O_3 + SO_4^{2-}$. The preservation of the fluorite framework despite extensive oxygen removal and sulfate incorporation demonstrates remarkable structural resilience, with sulfate species presumably occupying oxygen vacancy sites or surface positions without disrupting the underlying crystal lattice.

The sulfurized cerium compounds formed require careful consideration of thermodynamic stability and experimental evidence. While $Ce(SO_4)_2$ and $Ce_2(SO_4)_3$ represent the thermodynamically stable phases, cerium uniquely does not form oxysulfate phases observed in other rare-earth elements.[40] Previous studies have identified cerium sulfate oxide ($Ce_2O_2SO_4$) containing Ce^{3+} as the primary product of CeO_2 sulfurization by SO_2.[41,42] Our observed Ce^{3+}/S ratio of ~1.7 closely approximates the theoretical value of 2.0 expected for $Ce_2O_2SO_4$ formation, strongly suggesting this phase as the dominant sulfurization product. The presence of isosbestic points during *in situ* XANES measurements provides definitive evidence for direct $CeO_2 \rightarrow Ce_2O_2SO_4$ transformation without detectable intermediates, supporting a concerted mechanism where lattice oxygen removal and sulfate incorporation occur simultaneously. This direct conversion pathway, accelerated by Pd but maintaining the same stoichiometry, underscores the fundamental nature of the CeO_2–SO_2 reaction.

4. Conclusions

This study employed comprehensive *in situ* XAFS spectroscopy combined with XRD and STEM-EDS characterization to elucidate the mechanistic pathways of SO_2-induced structural transformations in Pd/CeO_2 catalysts. SO_2 treatment of bare CeO_2 at 500 °C induces surface-limited sulfurization with $Ce^{4+} \rightarrow Ce^{3+}$

reduction reaching a plateau at $Ce^{3+}/(Ce^{3+} + Ce^{4+}) = 0.18$. The presence of Pd fundamentally alters this behavior, enabling SO_2 penetration into the bulk lattice and achieving a $Ce^{3+}/(Ce^{3+} + Ce^{4+})$ ratio of 0.68 after 300 min. This sulfurized state proves remarkably stable, showing no re-oxidation upon O_2 exposure at 500 °C. Throughout the treatment, Pd remains oxidized and uniformly distributed without sintering, indicating that Pd promotes oxygen mobility rather than directly participating in sulfur chemistry. The primary product, $Ce_2O_2SO_4$, preserves the fluorite framework but exhibits diminished long-range order. These findings establish that Pd transforms the sulfurization mechanism from surface-limited to bulk-accessible while maintaining the structural architecture of CeO_2.

Conflicts of interest

There are no conflicts of interest to declare.

Data availability

The data supporting the findings of this study are available within the article and its supplementary information files. Additional raw data, including XAFS spectra, XRD patterns, and XPS measurements, are available from the corresponding author upon reasonable request. No restrictions apply to data sharing.

Acknowledgements

The authors gratefully acknowledge the support of this research from JST SICORP JPMJSC18H3 and JSPS KAKENHI Grant Number 21H03635. Parts of the XAFS experiments were performed at Kyushu University Beamline (SAGA-LS / BL06) with the proposal No. 2020IIK006.

References

1 J. Wang, H. Chen, Z. Hu, M. Yao and Y. Li, *Catal. Rev.*, 2015, **57**, 79–144.
2 M. A. van Spronsen, J. W. M. Frenken and I. M. N. Groot, *Chem. Soc. Rev.*, 2017, **46**, 4347–4374.
3 D. Ciuparu, M. R. Lyubovsky, E. Altman, L. D. Pfefferle and A. Datye, *Catal. Rev.*, 2002, **44**, 593–649.
4 R. M. Heck and R. J. Farrauto, *Appl. Catal., A*, 2001, **221**, 443–457.
5 Y. Ryou, J. Lee, H. Lee, J. W. Choung, S. Yoo and D. H. Kim, *Catal. Today*, 2015, **258**, 518–524.
6 M. Kaneeda, H. Iizuka, T. Hiratsuka, N. Shinotsuka and M. Arai, *Appl. Catal., B*, 2009, **90**, 564–569.
7 M. Chen and L. D. Schmidt, *J. Catal.*, 1979, **56**, 198–218.
8 C. H. Bartholomew, *Appl. Catal., A*, 2001, **212**, 17–60.
9 P. Gélin and M. Primet, *Appl. Catal., B*, 2002, **39**, 1–37.
10 S. Colussi, F. Arosio, T. Montanari, G. Busca, G. Groppi and A. Trovarelli, *Catal. Today*, 2010, **155**, 59–65.
11 H. S. Gandhi and M. Shelef, *Appl. Catal.*, 1991, **77**, 175–186.
12 F. Pinna, F. Menegazzo, M. Signoretto, P. Canton, G. Fagherazzi and N. Pernicone, *Appl. Catal., A*, 2001, **219**, 195–200.
13 M. Monai, T. Montini, M. Melchionna, T. Duchoň, P. Kúš, C. Chen, N. Tsud, L. Nasi, K. C. Prince, K. Veltruská, V. Matolín, M. M. Khader, R. J. Gorte and P. Fornasiero, *Appl. Catal., B*, 2017, **202**, 72–83.
14 S. P. Chenakin, G. Melaet, R. Szukiewicz and N. Kruse, *J. Catal.*, 2014, **312**, 1–11.
15 N. M. Kinnunen, J. T. Hirvi, K. Kallinen, T. Maunula, M. Keenan and M. Suvanto, *Appl. Catal., B*, 2017, **207**, 114–119.
16 T. Kolli, M. Huuhtanen, A. Hallikainen, K. Kallinen and R. L. Keiski, *Catal. Lett.*, 2009, **127**, 49–54.
17 H. Yang, G. Wei, X. Wang, F. Lin, J. Wang and M. Shen, *Catal. Commun.*, 2013, **36**, 5–9.
18 T. Luo and R. J. Gorte, *Appl. Catal., B*, 2004, **53**, 77–85.
19 R. Flouty, E. Abi-Aad, S. Siffert and A. Aboukaïs, *J. Therm. Anal. Calorim.*, 2003, **73**, 727–734.
20 X. Liu, P. Wang, Y. Shen, S. Bi, W. Ren and D. Zhang, *ACS Catal.*, 2022, **12**, 11306–11317.
21 S. Hilaire, S. Sharma, R. J. Gorte, J. M. Vohs and H.-W. Jen, *Catal. Lett.*, 2000, **70**, 131–135.
22 B. Ravel and M. Newville, *J. Synchrotron Radiat.*, 2005, **12**, 537–541.
23 A. V. Soldatov, T. S. Ivanchenko, S. Della Longa, A. Kotani, Y. Iwamoto and A. Bianconi, *Phys. Rev. B: Condens. Matter Mater. Phys.*, 1994, **50**, 5074.
24 P. Nachimuthu, W.-C. Shih, R.-S. Liu, L.-Y. Jang and J.-M. Chen, *J. Solid State Chem.*, 2000, **149**, 408–413.
25 H. Dexpert, R. C. Karnatak, J.-M. Esteva, J. P. Connerade, M. Gasgnier, P. E. Caro and L. Albert, *Phys. Rev. B:Condens. Matter Mater. Phys.*, 1987, **36**, 1750–1753.
26 J. Ke, W. Zhu, Y. Jiang, R. Si, Y.-J. Wang, S.-C. Li, C. Jin, H. Liu, W.-G. Song, C.-H. Yan and Y.-W. Zhang, *ACS Catal.*, 2015, **5**, 4884–4892.
27 L. Sun, X. Huang, L. Wang and A Janotti, *Phys. Rev. B*, 2017, **95**, 245101.
28 C. Macchi, A. M. S. Procópio, L. S. R. Rocha, P. P. Ortega, C. M. Aldao, L. I. Granone, H. M. S. Nascimento, M. S. Castro, F. D. Ivorra, A. Somoza, F. Moura and M. A. Ponce, *ACS Omega*, 2024, **9**, 42172–42182.
29 S. Shigenobu, H. Hojo and H. Einaga, *Ind. Eng. Chem. Res.*, 2022, **61**, 15856–15865.
30 P. Fornasiero, G. Balducci, R. Di Monte, J. Kašpar, V. Sergo, G. Gubitosa, A. Ferrero and M. Graziani, *J. Catal.*, 1996, **164**, 173–183.
31 M. Romeo, K. Bak, J. El Fallah, F. Le Normand and L. Hilaire, *Surf. Interface Anal.*, 1993, **20**, 508–512.
32 P. W. Park and J. S. Ledford, *Langmuir*, 1996, **12**, 1794–1799.
33 E. Bêche, P. Charvin, D. Perarnau, S. Abanades and G. Flamant, *Surf. Interface Anal.*, 2008, **40**, 264–267.

34 C. de Leitenburg, A. Trovarelli and J. Kašpar, *J. Catal.*, 1997, **166**, 98–107.
35 Y. Xu, M. Yamazaki and P. Villars, *Jpn. J. Appl. Phys.*, 2011, **50**, 11RH02.
36 S.-H. Oh and G. B. Hoflund, *J. Phys. Chem. A*, 2006, **110**, 7609–7613.
37 M.-F. Luo, Z.-Y. Hou, X.-X. Yuan and X.-M. Zheng, *Catal. Lett.*, 1998, **50**, 205–209.
38 M. Waqif, P. Bazin, O. Saur, J. C. Lavalley, G. Blanchard and O. Touret, *Appl. Catal., B*, 1997, **11**, 193–205.
39 A. Bianconi, A. Marcelli, H. Dexpert, R. Karnatak, A. Kotani, T. Jo and J. Petiau, *Phys. Rev. B:Condens. Matter Mater. Phys.*, 1987, **35**, 806–812.
40 R. K. Dwivedi and D. A. R. Kay, *Metall. Trans. B*, 1984, **15**, 523–528.
41 M. Y. Smirnov, A. V. Kalinkin, A. V. Pashis, A. M. Sorokin, A. S. Noskov, K. C. Kharas and V. I. Bukhtiyarov, *J. Phys. Chem. B*, 2005, **109**, 11712–11719.
42 M. Y. Smirnov, A. V. Kalinkin, A. V. Pashis, I. P. Prosvirin and V. I. Bukhtiyarov, *J. Phys. Chem. C*, 2014, **118**, 22120–22135.